chemistry

MDPI

Article

Raman Activities of Cyano-Ester Quinoidal Oligothiophenes Reveal Their Diradical Character and the Proximity of the Low-Lying Double Exciton State

Yasi Dai [1], Laura Bonometti [1], José Luis Zafra [2], Kazuo Takimiya [3,4,5], Juan Casado [2,*] and Fabrizia Negri [1,6,*]

[1] Dipartimento di Chimica 'Giacomo Ciamician', Università di Bologna, Via F. Selmi 2, 40126 Bologna, Italy; yasi.dai2@unibo.it (Y.D.); laura.bonometti@studio.unibo.it (L.B.)
[2] Department of Physical Chemistry, University of Málaga, Campus de Teatinos s/n, 29071 Málaga, Spain; zafra@uma.es
[3] RIKEN Center for Emergent Matter Science (CEMS), Wako 351-0198, Saitama, Japan; takimiya@riken.jp
[4] Department of Chemistry, Graduate School of Science, Tohoku University, Sendai 980-8578, Japan
[5] Advanced Institute for Materials Research, Tohoku University (WPI-AIMR), Sendai 980-8577, Japan
[6] INSTM, UdR Bologna, Via F. Selmi, 2, 40126 Bologna, Italy
* Correspondence: casado@uma.es (J.C.); fabrizia.negri@unibo.it (F.N.)

Abstract: Quinoidal oligothiophenes have received considerable attention as interesting platforms with remarkable amphoteric redox behavior associated with their diradical character increasing with the conjugation lengths. In this work, we considered a family of quinoidal oligothiophenes bearing cyano-ester terminal groups and characterized them by UV-Vis-NIR absorption and Raman spectroscopy measurements at different excitation wavelengths. The experimental investigation is complemented by quantum-chemical studies to assess the quality of computed density functional theory (DFT) ground state structures and their influence on predicted Raman intensities. In addition, resonance conditions with the optically active HOMO→LUMO transition as well as with the more elusive state dominated by the doubly excited HOMO,HOMO→LUMO,LUMO configuration, are determined with DFT-MRCI calculations and their contributions to Raman activity enhancement are discussed in terms of computed vibrational Huang–Rhys (HR) factors.

Keywords: conjugated diradicals; organic semiconductors; DFT; DFT-MRCI; Raman spectroscopy; resonance Raman enhancement; UV-Vis spectroscopy; excited electronic states; Huang–Rhys factors

Citation: Dai, Y.; Bonometti, L.; Zafra, J.L.; Takimiya, K.; Casado, J.; Negri, F. Raman Activities of Cyano-Ester Quinoidal Oligothiophenes Reveal Their Diradical Character and the Proximity of the Low-Lying Double Exciton State. *Chemistry* **2022**, *4*, 329–344. https://doi.org/10.3390/chemistry4020025

Academic Editor: Bartolo Gabriele

Received: 29 March 2022
Accepted: 14 April 2022
Published: 15 April 2022

1. Introduction

Recently, there has been an increased interest in designing stable conjugated diradicaloids with a singlet ground state and variable diradical character. These species have several potential technological applications ranging from spintronics to optoelectronics owing to their distinctive electrooptical properties [1–5]. Quinoidal oligothiophenes display increasing diradical character with the extension of the conjugated core and have been extensively investigated experimentally, owing to their relevant figures of merit and potential applications in the field of organic optoelectronics as electron-conducting or ambipolar materials. In this regard, the family of tetracyanoquinodimethane (TCNQ) quinoidal oligothiophenes has offered an interesting new platform with remarkable amphoteric redox behavior [6–15].

Among experimental investigations, vibrational spectroscopy and especially Raman spectroscopy characterization stands out for the wealth of information gathered, complemented by the results of computational studies [6,16–23]. Raman spectroscopy has been the technique of choice in the studies of the molecular and electronic structures of π-conjugated molecules. Particularly, in the case of quinoidal oligomers, Raman spectroscopy proved to be very useful, not only as an identification technique of their existence, but also as a source of information to get insight on their structures.

The most-intense Raman band in oligothiophenes and quinoidal oligothiophenes is due to a collective mode (the effective conjugation coordinate (ECC) involving the out-of-phase stretching between adjacent C-C and C=C bonds along the conjugation core [24–26]). Notably, this mode corresponds also to the out-of-phase C-C/C=C vibration responsible for the Franck-Condon activity in the electronic spectra of oligoenes [27,28] and oligothiophenes [29]. The Raman active modes dominated by the ECC coordinate are sensitive to geometry change. In fact, it has been shown that the evolution of the most intense Raman band when increasing the length of the quinoidal oligothiophenes, drastically differs from that recorded for a series of aromatic oligothiophenes: it downshifts from dimer to tetramer [17] with tetramer behaving as an inflection point after which the active frequency upshifts as a result of the aromatization of the ground electronic state.

The ground state structural information of conjugated diradicals derived by Raman investigations is generally well supported by quantum-chemical studies of equilibrium structures and computed Raman activities, especially for small to moderate diradical character [17–20,22,30]. The correct prediction of Raman intensities for conjugated diradicals is not, however, a trivial problem. Owing to the small HOMO-LUMO gap, the electronic structure of open shell singlet diradicals is significantly influenced by the role of static electron correlation and multi-reference computational methods should be employed [22,31]. However, due to the computational cost, a widely adopted practice to describe the singlet ground state of these species is based on the use of spin-unrestricted density functional theory (UDFT) [32]. In practice, when an instability of the restricted DFT (RDFT) closed-shell (CS) solution is found, a lower energy open-shell UDFT solution, characterized by broken symmetry (BS) frontier molecular orbitals, can be determined. Using UDFT, the corresponding BS optimized geometry can also be determined, providing generally a more realistic description of the diradical molecule, compared to the CS structure. The quality of computed Raman activities is, however, tightly connected with the quality of computed equilibrium structures and the predicted BS geometries not always provide satisfactory results since large diradical characters demand for multireference highly correlated wavefunctions. Thus, single-reference methods such as UDFT may lead to an unbalanced prediction of the open-shell structure, a result that may be influenced also by the functional chosen.

A recent combined experimental and computational study [30] further clarifies the above concept. In that work [30], it was shown that long rylenes, models for graphene nanoribbons, disclose their polyacetylenic character through the presence of Raman activity typical of polyenes. The observed Raman signatures were interpreted as due to an ECC vibration localized on the long edges of the extended rylene oligomers, developing as a result of their increased diradical character. In such case, the computed BS to CS geometry change, overlapping with the ECC coordinate, was correctly but not quantitatively captured by the UDFT calculations. Because small geometry deviations imply remarkable differences in computed vibrational frequencies and Raman activities [22], the quantitative prediction of the latter, for the longer members of the rylene family, required an *educated* molecular structure, obtained by displacing the geometry along the predicted BS-CS geometry change [30]. The above example shows that an assessment of the quality of RDFT/UDFT computed geometries is required for extended core conjugated diradicaloids, to ultimately predict the evolution of Raman spectra for increasing diradical characters. Furthermore, ad hoc adjustments of predicted geometries might be required and must be interpreted as required to compensate for the missing static electron correlation at DFT level.

An additional source of information, intrinsic in measured Raman spectra, is provided by the enhancement effects appearing when the laser light is in resonance or pre-resonance with one or more specific electronic transitions [33–35]. In this context, it is worth noting that at least two excited states of singlet multiplicity may contribute to the absorption spectra of conjugated diradicaloids: one dominated by the HOMO→LUMO single excitation and one dominated by the HOMO,HOMO→LUMO,LUMO double excitation [22,31,36–39], hereafter labelled the DE state. Thus, because most conjugated diradical molecules are char-

acterized by a low-lying double-exciton (DE) state, Raman intensities may be modulated not only by resonance with the optically active HOMO→LUMO transition, but also by the proximity of the less active DE state.

Prompted by the above two challenging issues, namely, the reliable prediction of Raman intensities for varying diradical characters and the assessment of resonance enhancement effects, in this work, we considered a family of quinoidal oligothiophenes bearing cyano (-CN) and ester (-$COOC_8H_{17}$) substituents as terminal groups (Figure 1) [40].

The three oligomers, labeled **EsQ2**, **EsQ3** and **EsQ4** because of the ester (Es) substituents and quinoidal (Q) structure, were characterized by UV-Vis-NIR absorption and Raman spectroscopy measurements at different excitation wavelengths. The experimental results are analyzed with the support of quantum-chemical investigations, aiming at assessing the quality of computed RDFT/UDFT ground state structures and their influence on predicted Raman intensities. In addition, resonance conditions with the bright HOMO→LUMO transition as well as the more elusive DE state, are determined and their contributions to Raman activity enhancement is discussed.

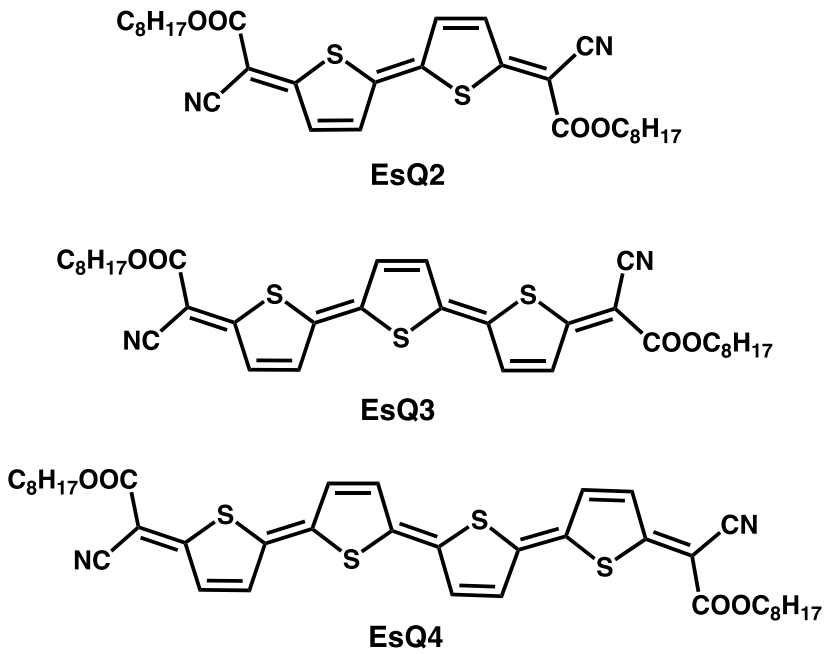

Figure 1. Chemical structure of cyano-ester quinoidal oligothiophenes.

2. Materials and Methods

2.1. Experimental Details

UV-vis-NIR spectra were recorded in dichloromethane in a 1 cm path-length quartz cell on an 845x UV-visible Agilent spectrophotometer (Malaga, Spain).

FT−Raman spectra were measured using an FT−Raman accessory kit (FRA/106−S) of a Bruker Equinox 55 FT−IR interferometer (Malaga, Spain). A continuous-wave Nd−YAG laser working at 1064 nm was employed for excitation, at a laser power in the sample not exceeding 20 mW. A germanium detector operating at liquid nitrogen temperature was used. Raman scattering radiation was collected in a back-scattering configuration with a standard spectral resolution of 4 cm^{-1}. 3000 scans were averaged for each spectrum.

Raman spectra with the excitation lasers at 532, 633 and 785 nm were collected by using the 1 × 1 camera of a Bruker Senterra Raman microscope by averaging spectra during 60 min, with a resolution of 3–5 cm^{-1}. A CCD camera operating at −50 °C was used for Raman detection.

2.2. Computational Details

Calculations were carried out on models of the real molecules, with methyl groups replacing the long alkyl chains of the ester groups (Figure 1). This is expected to reduce the number of Raman active vibrational frequencies but because the most active vibrations involve the conjugated skeleton, such simplification leaves untouched by the molecular moiety and the π–electronic structure responsible for Raman enhancement. Because the terminal ester groups are flexible, two conformers (*Conf1* and *Conf*2, Figure S1) characterized by the different orientations of the ester groups with respect to the nearby thiophene ring were initially considered.

A library of different geometries for each oligomer was generated by determining optimized structures with Density Functional Theory (DFT) and Hartree-Fock (HF) theory, in conjunction with the 6-31G* basis set. Two functionals—CAM-B3LYP and B3LYP—were selected, owing to their different bond-length alternation predictions in conjugated hydrocarbons. DFT and HF geometry optimizations were carried out in the restricted formulation and, when a wavefunction instability was found, the unrestricted approach was also employed to determine the BS optimized geometry. The nature of the stationary points was assessed by computing vibrational frequencies.

Overall, up to six geometries for each molecule were determined: three from the CS approach and three from the BS approach, hereafter identified by the CS-/BS- prefix followed by the level of theory (Figures S2–S4). The optimized geometries forming the set for each oligomer are indicated in Table S1 along with the energy difference between the two conformers. The remarkably larger stabilization of *Conf 2* can be traced back to the stronger through space electrostatic interaction between sulfur and the carbonyl oxygen [41]. Hereafter, we will therefore consider only *Conf 2*.

To explore the dependence of computed vibrational frequencies and Raman intensities on structural parameters, the Raman spectrum was simulated for each optimized geometry, at B3LYP/6-31G* level and vibrational frequencies were scaled by 0.97, since a very close match with experimental vibrational frequencies and intensities was previously demonstrated at this level of theory. We adopted a similar approach in previous works [22,30] and we showed that for frequencies above 1000 cm^{-1} the Raman activities are reliably described even if the geometry used is not a minimum for the level of theory employed. All the above calculations were carried out with the Gaussian 16 package [42].

The electronic absorption spectra of cyano-ester quinoidal oligothiophenes were investigated by time dependent (TD) DFT calculations and, to determine the energy location of the DE state, DFT-MRCI calculations were also carried out taking as reference the CS-B3LYP geometries for **EsQ2** and **EsQ3** and the BS-UB3LYP for **EsQ4**. The DFT-MRCI method employs DFT orbitals (BHLYP functional) for constructing configuration state functions (CSFs) and dresses the MRCI matrix elements by appropriate portions of Coulomb and exchange-like integrals and allows to describe excited electronic states dominated by doubly excited configurations. The spin-invariant parametrization was used [43].

Each computed geometry was characterized by its diradical character, evaluated using two descriptors: y_0 and N^{FOD}. The y_0 index was calculated at the PUHF/6-31G * level of theory, following Yamaguchi's approach in the spin-projection scheme as [44]:

$$y_0^{PUHF} = 1 - \frac{2T_0}{1 + T_0^2} \quad (1)$$

with T_0 calculated as:

$$T_0 = \frac{n_{HONO} - n_{LUNO}}{2} \quad (2)$$

where n_{HONO} and n_{LUNO} are the occupation number of the highest occupied (HONO) and lowest unoccupied (LUNO) natural orbitals, respectively.

The N^{FOD} value is based on finite-temperature DFT (FT-DFT) and describes also eventual multiradical character. It is obtained by integrating the fractional orbital density function (ρ^{FOD}) over all space. ρ^{FOD} is evaluated as follow:

$$\rho^{FOD}(r) = \sum_{i}^{N} (\delta_1 - \delta_2 f_i) |\varphi_i(r)|^2 \quad (3)$$

where δ_1 and δ_2 are two constants and are set such that only fractional occupied orbitals are considered; φ_i are molecular spin orbitals and f_i are the fractional orbital occupations ($0 \leq f_i \leq 1$) determined by the Fermi–Dirac distribution:

$$f_i = \frac{1}{e^{(\varepsilon_i - \varepsilon_F)/kT_{el}} + 1} \quad (4)$$

N^{FOD} was calculated with the ORCA 4.0.1.2 package [45] with the default setting (TPSS/def2- TZVP level with T_{el} = 5000 K).

To model resonance Raman spectra, we considered the ground state equilibrium structure used to model off-resonance Raman intensities and we additionally computed the equilibrium structure of the optically allowed excited state (Figure S5). The geometry change was projected onto ground state vibrational normal coordinates to evaluate dimensionless displacement parameters as outlined in the following. The geometry of the DE state cannot be obtained by TDDFT calculations owing to its multi-exciton nature [22,31]. However, we have previously shown that the BS-CS geometry change overlaps with the ECC coordinate and with both the ground to optically active state geometry change and the ground to DE geometry change [22,30,31]. Thus, we can safely assume that Raman enhanced modes associated with resonance with the DE state are expected to be similar to those active in the optically allowed state. Under the assumption of resonance with the 0-0 band of the $S_0 \rightarrow S_n$ transition, the activity of each totally symmetric vibration in resonance Raman spectra is proportional [33] to the Huang–Rhys (HR) factor S_k [46,47] for each vibrational mode k with frequency ν_k. Each S_k was obtained as

$$S_k = \frac{1}{2} {B_k}^2 \quad (5)$$

where B_k is the dimensionless displacement parameter defined assuming the harmonic approximation, as

$$B_k = \sqrt{\frac{2\pi\nu_k}{\hbar}} [\boldsymbol{X_j} - \boldsymbol{X_i}] \boldsymbol{M}^{\frac{1}{2}} \boldsymbol{Q}_k(j) \quad (6)$$

where $\boldsymbol{X}_{i,j}$ is the $3N$ dimensional vector of the equilibrium Cartesian coordinates of the i, j electronic state (here i is the excited electronic state and j is the ground state), $\boldsymbol{M}$ is the $3N \times 3N$ diagonal matrix of atomic masses and $\boldsymbol{Q}_k(j)$ is the $3N$ dimensional vector describing the k normal coordinate of the j (ground) state in terms of mass weighted Cartesian coordinates.

3. Results and Discussion

3.1. The Library of Ground State Geometries and Their Associated Diradical Character

In this section, we discuss the distinctive features of the ground state structures optimized at different levels of theory. The diradical character of each generated geometry is determined by evaluating the associated y_0^{PUHF} (Table 1) and N^{FOD} (Table S2) values.

As can be seen, for a given oligomer, both y_0 and N^{FOD} increase from CS-HF to BS-UHF with intermediate values for CS- and BS-DFT geometries. The only exception is **EsQ4**, the highest y_0 value of which is found for the BS-UCAM-B3LYP geometry. Notably, B3LYP and CAM-B3LYP functionals return different y_0 or N^{FOD} values, indicating a functional dependent diradical character description of predicted ground state structures. An increased diradical character is expected when moving from CS to BS geometries, but the amount

of HF exchange also plays a role, with smaller y_0^{PUHF} values computed for CS-HF and CS-CAM-B3LYP geometries as compared to CS-B3LYP and the opposite for BS geometries.

Table 1. y_0^{PUHF} calculated at different optimized geometries of **EsQ2, EsQ3 and EsQ4**.

	y_0^{PUHF}					
Geometry →	**CS-HF**	**CS-CAM-B3LYP**	**CS-B3LYP**	**BS-UB3LYP**	**BS-UCAM-B3LYP**	**BS-UHF**
Molecule ↓						
EsQ2	0.14	0.21	0.27	/	/	0.39
EsQ3	0.22	0.31	0.41	/	0.50	0.56
EsQ4	0.28	0.42	0.54	0.64	0.73	0.69

As expected, for a fixed level of theory, e.g., CS-B3LYP, the predicted diradical descriptors (both y_0 and N^{FOD}) increase with the conjugation length (i.e., from **EsQ2** to **EsQ4**). Given the similar trend of the two diradical indexes, we will refer only to y_0^{PUHF} values in the remaining discussion.

Since the diradical character of quinoidal oligothiophenes is associated with a recovery of aromaticity, the varying y_0^{PUHF} values computed for the same oligomer at different levels of theory, ultimately reflect a different CC bond length alternation along the conjugated chain, as can be clearly seen in Figure 2 for **EsQ4** and Figures S6 and S7 for shorter oligomers. All CS geometries show a more marked CC bond length alternation compared to the corresponding BS geometries, highlighting a more quinoidal structure for the former. A smaller amount of HF exchange implies a reduced bond-length alternation for CS-structures but also a reduced CS-BS geometry change. Thus, larger CS-BS bond-length alternation changes are predicted at CAM-B3LYP level and this leads, for **EsQ4**, to the largest recovery of aromaticity predicted by the BS-UCAM-B3LYP geometry (see also Figures S2–S4).

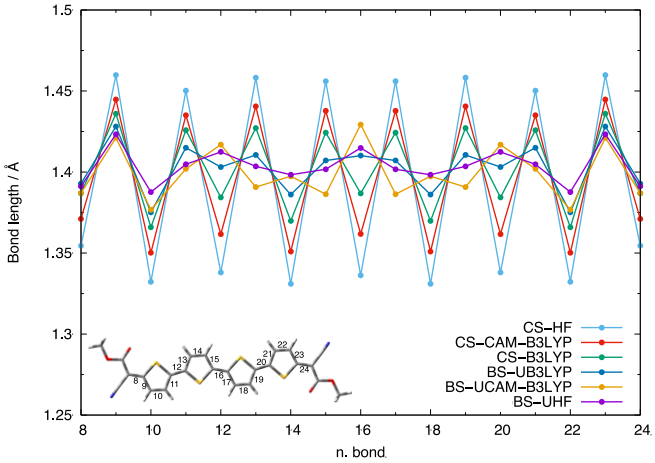

Figure 2. **EsQ4** CC bond lengths calculated at CS-HF (cyan), CS-CAM-B3LYP (red), CS-B3LYP (green), BS-UB3LYP (blue), BS-UCAM-B3LYP (orange) and BS-UHF (purple) geometries. Bottom left: definition of bond numbers.

The tight correlation between CC bond-lengths belonging to the central conjugated core and diradical character is highlighted in Figure 3a for **EsQ2** and Figure S8 for **EsQ3** and **EsQ4**. The very good linear relationship suggests that these bonds are diagnostic of the diradical character, in contrast to other bond lengths such as C=O and C≡N (Figures 3b and S9).

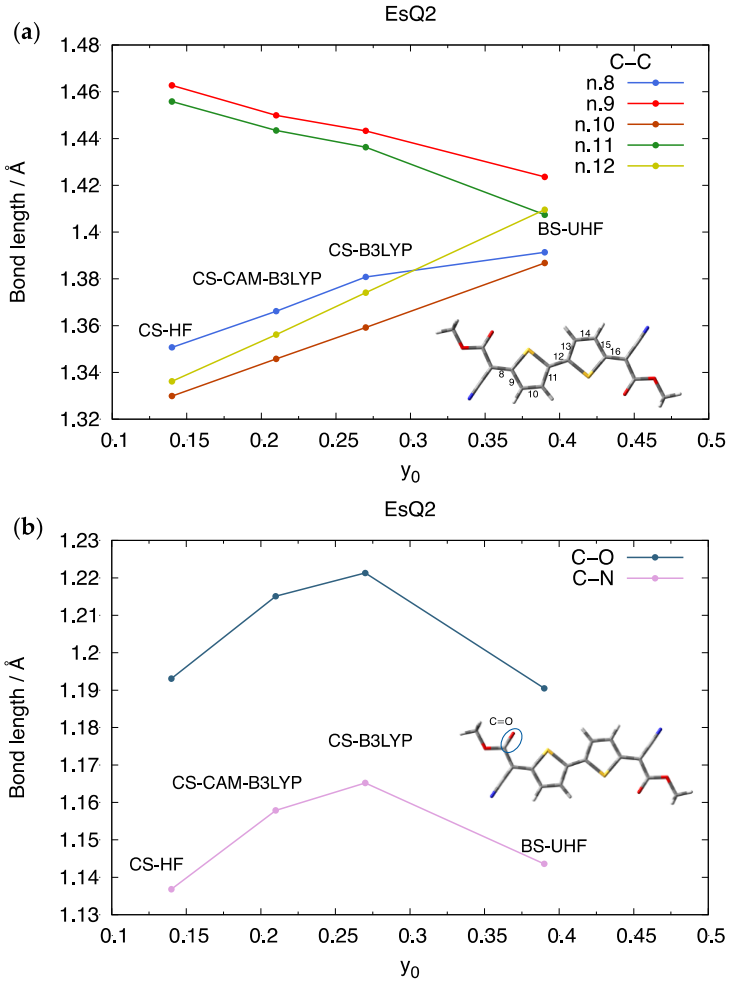

Figure 3. Correlation between y_0^{PUHF} and C-C bond lengths (**a**) and C≡N/C=O bond lengths (**b**) of **EsQ2** calculated at different geometries: CS-HF, CS-CAM-B3LYP, CS-B3LYP and BS-UHF. Bottom right of (**a**): definition of bond number; Center right of (**b**): C=O bond considered in this figure.

3.2. Absorption Spectra and Low-Lying Excited Electronic States

The experimental UV-Vis-NIR absorption spectra of the three oligomers are shown in Figure 4. These spectra, as those of the corresponding TCNQ derivatives [10,17], display additional spectral features on the red side of the main absorption maximum, which are suggestive of vibronic transitions to the DE state, previously identified for several conjugated diradicals [31,38,48]. For centrosymmetric molecules the electronic transition to the DE state is symmetry forbidden. However, it may acquire intensity according to the Herzberg–Teller (HT) mechanism of intensity borrowing [49]. Small deviations from centrosymmetric symmetry due to conformational flexibility may also break the selection rule and these mechanisms explain why such weak features appear in the spectra.

Because some experimental Raman spectra were obtained for different excitation wavelengths, we investigated computationally the low-lying excited states that may be responsible for enhancing selected vibrational bands [35]. In contrast to TDDFT calculations that correctly capture only the strongly optically active HOMO→LUMO transition, (frontier molecular orbitals in Figures S10 and S11) DFT-MRCI calculations show clear evidence of a low-lying DE state for all the oligomers investigated, computed to be the second lowest excited state for **EsQ2** and the lowest excited state for **EsQ3** and **EsQ4** at their ground state geometries (Table 2), in agreement with recent analysis of the absorption spectra of related quinoidal oligothiophene trimers [15]. The computed DFT-MRCI excitation energies are shown as red (DE state) and green (HOMO→LUMO state) bars over the (black)

experimental absorption spectra in Figure 4. Notably, experimentally, there is no clear evidence of such DE state in **EsQ2** since its transition overlaps with the strongly optically active HOMO→LUMO excitation. In contrast, a clear shoulder on the low energy side (673 nm) of **EsQ3** may be assigned to a vibronically activated transition to the DE state as well as the weak features at 851 and ca. 940 nm in the spectrum of **EsQ4**.

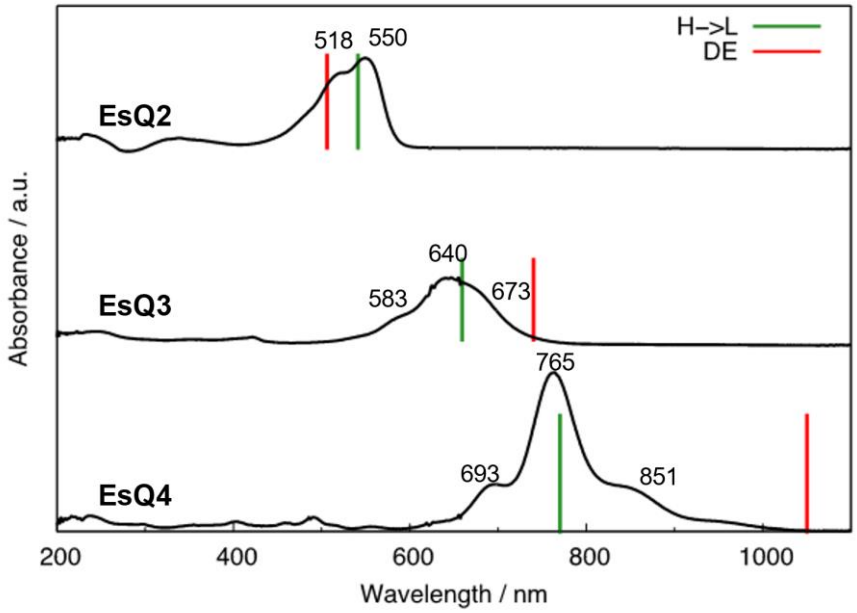

Figure 4. Comparison between UV-Vis-NIR electronic absorption spectra of cyano-ester quinoidal oligothiophenes in dichloromethane (solid black lines and black numbers) and DFT-MRCI computed excitation energies for the bright HOMO→LUMO (green bars) and the DE (red bars) electronic states.

Thus, DFT-MRCI calculations help clarifying when measured Raman spectra may be affected by resonance or pre-resonance not only with the strongly optically active HOMO→LUMO state, but also with the more elusive DE state.

Table 2. Computed DFT-MRCI excitation energies of the optically active HOMO→LUMO transition and of the DE state and comparison with observed peaks in absorption spectra of **EsQn** oligomers.

Molecule ↓	Excited Electronic State	Calc (eV)	Calc (nm)	Exp (nm)
EsQ2	H→L	2.29	541	550
	DE	2.45	506	-
EsQ3	DE	1.67	740	750 *
	H→L	1.88	659	640
EsQ4	DE	1.18	1050	1050 *
	H→L	1.61	770	765

* onset of the absorption spectrum.

3.3. Experimental and Simulated Raman Spectra

According to the discussion above, the comparison between computed and observed Raman spectra must consider, on one side, the level of theory dependence of computed Raman bands, due to the different diradical character of predicted ground state structures and, on the other side, the effects of resonance enhancement that may be induced by the proximity of allowed or HT induced electronic transitions [33–35]. Thus, first we compare for each oligomer, the (off-resonance) Raman intensities computed for each member of the set of ground state structures with the observed off-resonance Raman spectra, to identify the most suitable level of theory for Raman activity prediction. Second, we discuss possible resonance enhancements based on computed HR parameters.

Of the four reported Raman spectra of **EsQ2** (Figure 5), the spectrum obtained by exciting at 532 nm is clearly in resonance with both the HOMO→LUMO and the DE transitions of **EsQ2**. Therefore, we compare the 1064 nm Raman spectrum (off-resonance) with those predicted by the set of ground state geometries (Figures 6 and S12). All display a dominant active frequency associated with the ECC coordinate (Figure S13) which, as expected, downshifts with the increasing diradical character of the predicted geometry. The best agreement is obtained by the Raman spectrum predicted at the CS-B3LYP geometry, whose computed active frequencies are in excellent agreement with the experimental result.

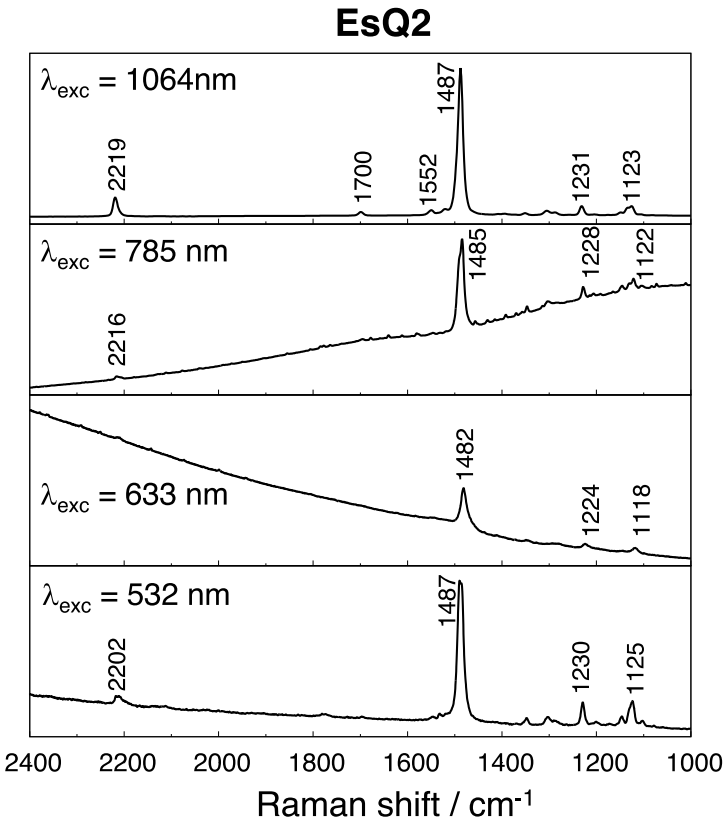

Figure 5. Raman spectra of **EsQ2** measured in the solid state at room temperature with different excitation wavelengths: from top to bottom: 1064 nm; 785 nm; 633 nm; 532 nm.

Moving now to resonance effects, we note that the HR factors computed for the optically active transition of **EsQ2** (Table 3) suggest Raman enhancement for the vibrations computed at 1118 cm^{-1}, 1229 cm^{-1} and 1495 cm^{-1}, in good agreement with the intensity increase of the corresponding 1125 cm^{-1}, 1230 cm^{-1} and 1487 cm^{-1} bands in the experimental spectrum measured by exciting at 532 nm (Figure 5). Notably, beside the ECC dominated mode at 1495 cm^{-1}, the 1229 cm^{-1} frequency mode also bears some contribution of out-of-phase adjacent C-C/C=C stretching in the central conjugated core (Figure S14). Furthermore, we show below that Raman enhancement due to these modes becomes more relevant for longer oligomers.

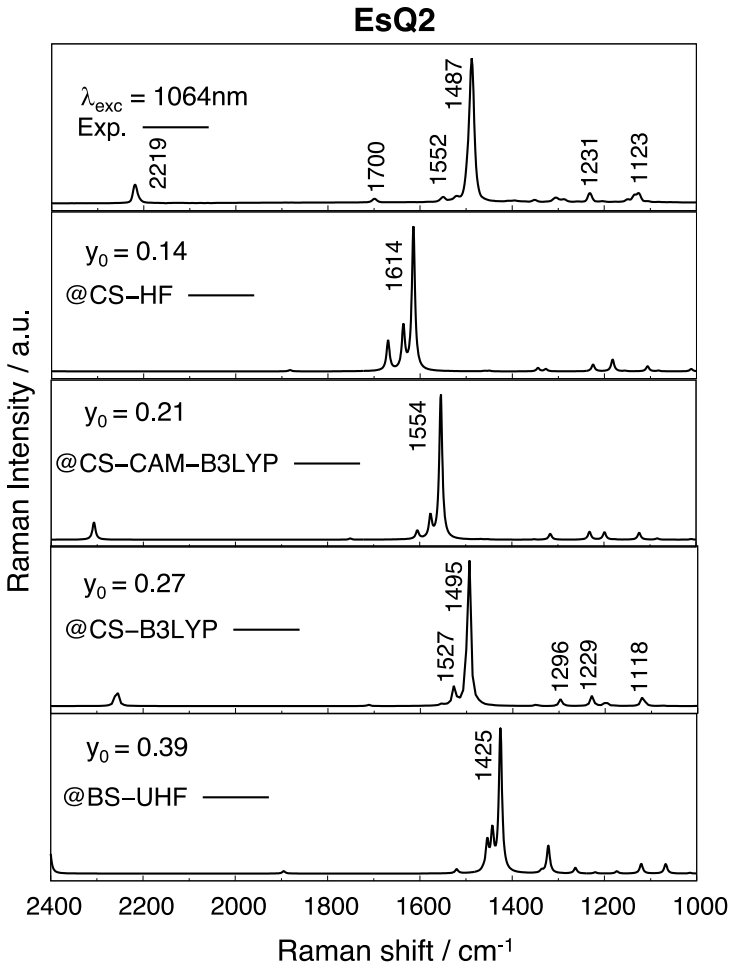

Figure 6. Comparison between experimental (top, spectrum measured at 1064 nm) and computed Raman spectra for the library of ground state geometries of **EsQ2** characterized by increasing diradical character as indicated in the top left part of each panel.

Table 3. Computed HR factors for the optically active transition of **EsQ2, EsQ3** and **EsQ4**.

EsQ2		EsQ3		EsQ4	
Frequency/cm^{-1}	**HR Factor [a]**	**Frequency/cm^{-1}**	**HR Factor [a]**	**Frequency/cm^{-1}**	**HR Factor [b]**
1118	0.0349	1096	0.0130	1046	0.0750
1198	0.0263	1120	0.0196	1249	0.0591
1229	0.0874	1203	0.0755	1301	0.0400
1296	0.0199	1225	0.0278	1316	0.0162
1495	0.2029	1447	0.1443	1322	0.1112
1527	0.0367	1447	0.0595	1385	0.0104
				1499	0.0017
				1516	0.0029

[a] Ground and excited states computed with the B3LYP functional. [b] Ground and excited state computed with the CAM-B3LYP functional.

The wavelength dependence of the Raman spectra of **EsQ3** and **EsQ4** (Figure 7) is more remarkable due to the red shift of the optically active transition and concomitant lowering of the DE state which may also influence the measured spectra. For **EsQ3** the spectrum measured exciting at 1064 nm can still be considered reasonably far from resonance and is therefore considered for comparison with the off-resonance Raman spectra predicted for the set of ground state geometries (Figure S15).

The most relevant change in computed Raman spectra is the downshift of the dominant active frequency (Figure S15) associated with the ECC coordinate (Figure S13), with the increasing diradical character of the predicted geometry. The best agreement is obtained by the Raman spectrum predicted either at the CS-B3LYP or the BS-UCAM-B3LYP geometries, displaying a comparable y_0 (0.41–0.50) and a similar trend in bond-length alternation although a more marked equalization is documented for the BS-UCAM-B3LYP structure (Figures S5 and S7). The computed dominant activity at 1447 cm^{-1} or 1419 cm^{-1} (due to the ECC mode), for CS-B3LYP or BS-UCAM-B3LYP geometries, is in comparable good agreement with the experimental most intense activity observed at 1425 cm^{-1}. The slight frequency overestimate at CS-B3LYP and slight underestimate at the BS-UCAM-B3LYP geometry might suggest that the correct ground state geometry of **EsQ3** lies midway between the two. These predictions confirm that CS-B3LYP is still a reliable ground state geometry for short to medium length quinoidal oligomers of **EsQn** (Figure 8a).

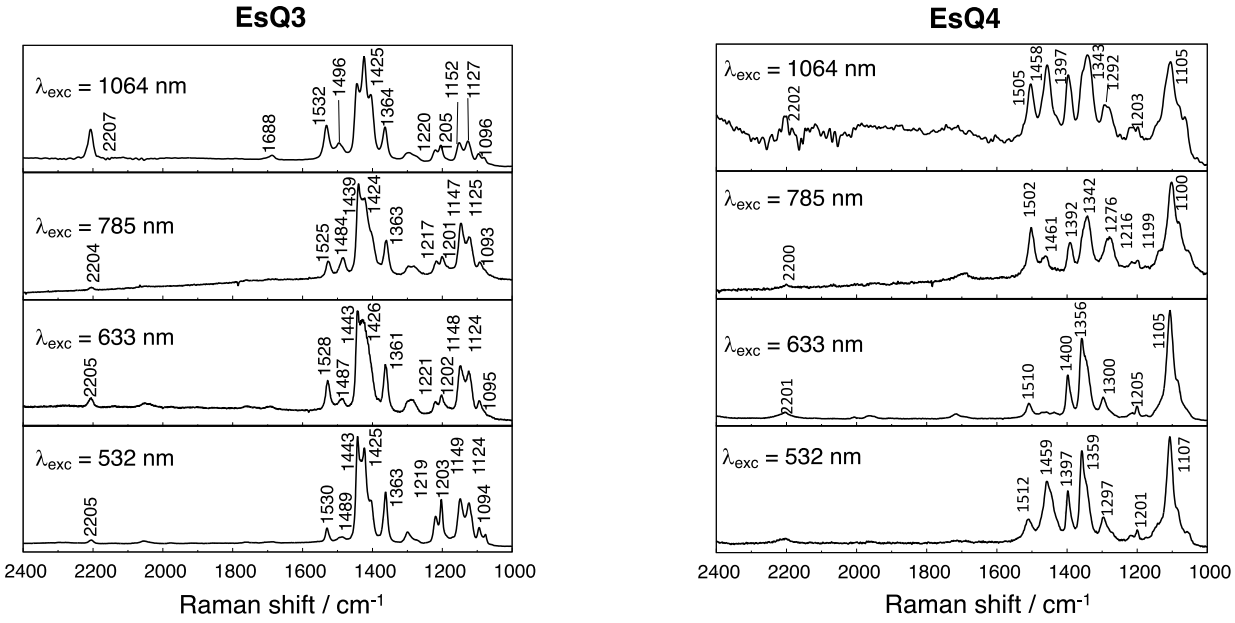

Figure 7. Raman spectra of **EsQ3** (**a**) and **EsQ4** (**b**) measured in the solid state at room temperature with different excitation wavelengths: from top to bottom: 1064 nm; 785 nm; 633 nm; 532 nm.

The HR parameters computed for the optically active transition of **EsQ3** (Table 3) suggest resonance Raman enhancement not only for the mode dominated by the ECC coordinate at 1447 cm^{-1}, but also for vibrations in the 1090–1230 cm^{-1} region (Figure S16), in nice agreement with the intensity increase observed for the Raman spectrum measured exciting in resonance (633 nm) and just above (532 nm) the optically active HOMO→LUMO state but also at 785 nm, which is in resonance with the DE state, implying intensity modulations driven also by the presence of such lower lying and weaker transition, as it has been previously reported for other HT induced transitions [35,50]. The out-of-phase adjacent C-C/C=C stretching contribution of some of the low frequency (<1300 cm^{-1}) active modes is even more marked for **EsQ3** compared to **EsQ2** and their intensity enhancement, associated to their relevant electron-phonon coupling, is rationalized by the nuclear displacements overlapping with the direction of the ground to excited state geometry change.

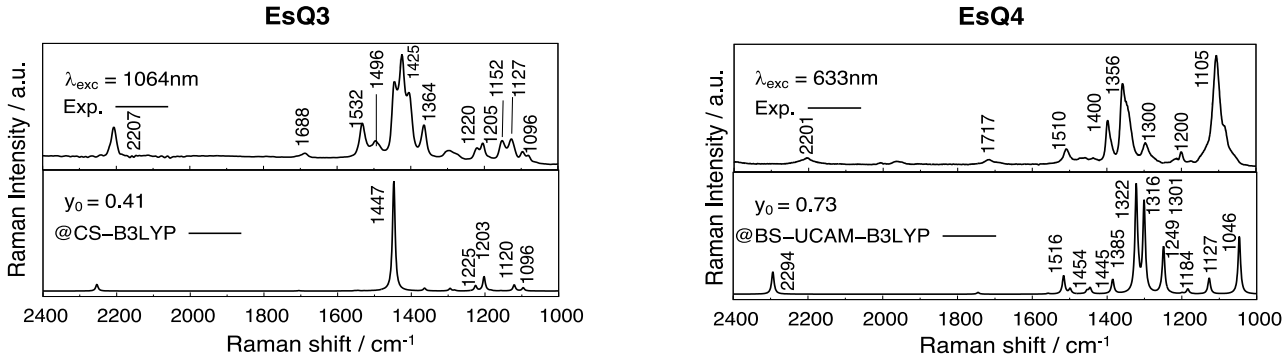

Figure 8. Comparison between computed (**bottom**) and observed (**top**) Raman spectra of **EsQ3** (**a**) and **EsQ4** (**b**). The ground state geometry used to simulate the spectra is indicated in each panel, along with the associated diradical character y_0.

Figures 5 and 7 show that increasing the conjugation length from **EsQ2** to **EsQ4** (and therefore, the diradical character) the high frequency active mode dominated by the ECC coordinate downshifts, as previously documented [17], since this mode is diagnostic of the diradical character. While the Raman activity below 1300 cm^{-1} is modest in **EsQ2**, its intensity contribution increases in **EsQ3**, most likely due to resonance effects as shown by computations. Interestingly, such low frequency activity becomes dominant in the Raman spectra of **EsQ4** (Figure 7b) at all exciting wavelengths. This can be justified by the computed excitation energies discussed in Section 3.2 (Figure 4), implying that resonance effects pervade the spectra measured with the highest two excitation wavelengths: at 1064 nm resonance with the DE state as suggested by calculations, while at 785 nm with the optically active HOMO→LUMO state, as proved by both computed and observed absorption spectra. Further resonance effects with specific vibronic levels of the optically active excited state cannot be ruled out in the spectra measured at 633 nm and 532 nm, as suggested by the intensity modulation of some bands around 1500 cm^{-1}. A comparison of the 633 nm Raman spectrum with those computed for the set of ground state geometries of **EsQ4** (Figure S17) reveals that the 633 nm spectrum is the less affected by resonance effects. The computed spectra show a downshift of the most intense Raman activity with increasing diradical character and a concomitant intensity redistribution on the higher and lower frequency regions with respect to the dominant ECC activity. This intensity remodulation induced by geometry changes, finds its closest agreement with the experimental data when the BS-UCAM-B3LYP geometry is employed (Figure 8b). Notably, this geometry shows a slight blue-shift of the most intense peak with respect to the corresponding peak calculated at the BS-UHF geometry, which precedes in the scale of diradical character (Figure S4). This minor blue-shift and increased diradical character can be traced back to the inverted bond-length alternation of the BS-UCAM-B3LYP geometry (Figure 2), compared to the remaining set of ground state geometries optimized for **EsQ4** and agrees with the previously reported inflection point after which the active Raman frequency upshifts, documented for TCNQ quinoidal thiophene tetramers [17]. The computed off-resonance Raman activity of the 1046 cm^{-1} frequency mode, associated with the band observed at ca. 1100 cm^{-1} and characterized by out-of-phase C-C/C=C stretching contributions (Figure 9), is slightly underestimated. Its stronger observed intensity can be reconciled when resonance effects are taken into account, as indicated by the remarkable HR factor computed for this vibration (Table 3), implying an additional intensity contribution via resonance with both the optically active and the DE state. Finally, we note that HR factors suggest some enhancement also for modes around 1500 cm^{-1}, which may explain the intensity modulation in this region as a function of exciting wavelength.

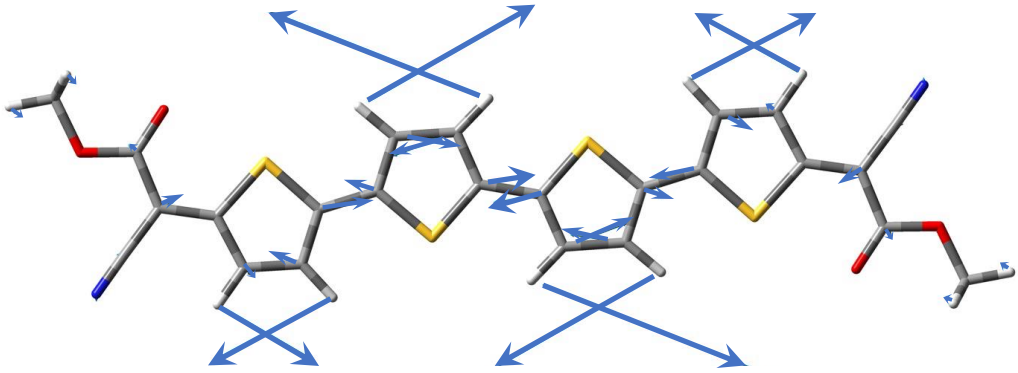

Figure 9. Vibrational mode of **EsQ4** computed at 1046 cm^{-1}, assigned to the observed peak at ca. 1100 cm^{-1} and displaying the largest HR factor among low frequency vibrations.

4. Conclusions

In this work, we investigated experimentally and with quantum-chemical calculations a family of quinoidal oligothiophenes bearing cyano-ester terminal groups which are characterized by a singlet ground state with increasing open-shell diradical character.

We explored the role of geometry predictions on computed Raman intensities by considering a library of ground state geometries generated with different levels of theory, with the aim of assessing to what extent the single reference description provided by RDFT/UDFT approaches may depend on the chosen functional and when the non-negligible contribution of static electron correlation becomes critical for the prediction of Raman activities. We showed that selected CC bond lengths along the conjugation path, predicted by different levels of theory, linearly depend on diradical character and can be assigned as bond lengths diagnostic of diradical character.

Concerning the functional dependence of predicted geometries and Raman activities, the study shows that the amount of HF exchange influences the predicted geometries. For the family of oligomers investigated here, the CS-B3LYP geometry and the associated Raman intensities are reliable for small to medium length conjugation. For the longer **EsQ4** oligomer, the BS-UCAM-B3LYP geometry is of superior quality compared to other ground state structures, as demonstrated by the good agreement of predicted vs experimental Raman spectrum. Notably, the predicted geometry of the **EsQ4** oligomer confirms its turning point nature, after which (i.e., for longer oligomers) the ECC dominated Raman active frequency upshifts.

Because experimental Raman spectra were obtained for different exciting wavelengths, we investigated the nature and excitation energy of the low-lying singlet excited states to assess the role of resonance effects and demonstrated, with DFT-MRCI calculations, that the DE state is only slightly above the optically active transition of **EsQ2,** while it is the lowest energy excited state for **EsQ3** and **EsQ4**.

The HR factors governing vibrational resonance enhancement were evaluated for the three oligomers and showed, in addition to the expected enhancement of the mode dominated by the ECC coordinate, an increasing contribution for vibrations with frequencies below 1300 cm^{-1}, bearing contributions from C-C/C=C stretching.

Overall, the combined experimental and computational investigation reveals an increasing Raman activity of low frequency vibrations associated with CC stretching modes that are further enhanced by resonance with both the optically active and the DE state, thereby demonstrating the additional potential of Raman spectroscopy in revealing signatures of the elusive double exciton state that distinctively characterizes conjugated diradicals.

Supplementary Materials: The following supporting information can be downloaded at: https://www.mdpi.com/article/10.3390/chemistry4020025/s1. Figures S1–S18 and Tables S1–S3.

Author Contributions: Conceptualization, F.N. and J.C.; synthesis, K.T.; investigation, Y.D., L.B., J.L.Z., K.T., F.N. and J.C.; writing—original draft preparation, Y.D.; writing—review and editing, Y.D., F.N. and J.C. All authors have read and agreed to the published version of the manuscript.

Funding: We thank MINECO/FEDER of the Spanish Government (project reference PGC2018-098533-B-100) and the Junta de Andalucía, Spain (UMA18FEDERJA057).

Institutional Review Board Statement: Not applicable.

Informed Consent Statement: Not applicable.

Data Availability Statement: Not applicable.

Acknowledgments: RFO funds from the University of Bologna and computational resources from CINECA through an ISCRA (Italian Super Computing Resource Allocation) C project are acknowledged. Y.D. acknowledges MIUR for her PhD fellowship. We also thank the vibrational spectroscopy unit of the Research Central Services (SCAI) of the University of Málaga.

Conflicts of Interest: The authors declare no conflict of interest.

References

1. Huang, Y.; Egap, E. Open-shell organic semiconductors: An emerging class of materials with novel properties. *Polym. J.* **2018**, *50*, 603–614. [CrossRef]
2. Hu, X.; Wang, W.; Wang, D.; Zheng, Y. The electronic applications of stable diradicaloids: Present and future. *J. Mater. Chem. C* **2018**, *6*, 11232–11242. [CrossRef]
3. Chen, Z.X.; Li, Y.; Huang, F. Persistent and Stable Organic Radicals: Design, Synthesis and Applications. *Chem* **2021**, *7*, 288–332. [CrossRef]
4. Dong, S.; Li, Z. Recent progress in open-shell organic conjugated materials and their aggregated states. *J. Mater. Chem. C* **2022**, *10*, 2431–2449. [CrossRef]
5. Abe, M. Diradicals. *Chem. Rev.* **2013**, *113*, 7011–7088. [CrossRef] [PubMed]
6. Ponce Ortiz, R.; Casado, J.; Hernández, V.; López Navarrete, J.T.; Ortí, E.; Viruela, P.M.; Milián, B.; Hotta, S.; Zotti, G.; Zecchin, S.; et al. Magnetic properties of quinoidal oligothiophenes: More than good candidates for ambipolar organic semiconductors? *Adv. Funct. Mater.* **2006**, *16*, 531–536. [CrossRef]
7. Pappenfus, T.M.; Chesterfield, R.J.; Frisbie, C.D.; Mann, K.R.; Casado, J.; Raff, J.D.; Miller, L.L. A π-Stacking Terthiophene-Based Quinodimethane Is an n-Channel Conductor in a Thin Film Transistor. *J. Am. Chem. Soc.* **2002**, *124*, 4184–4185. [CrossRef]
8. Janzen, D.E.; Burand, M.W.; Ewbank, P.C.; Pappenfus, T.M.; Higuchi, H.; da Silva Filho, D.A.; Young, V.G.; Brédas, J.-L.; Mann, K.R. Preparation and Characterization of π-Stacking Quinodimethane Oligothiophenes. Predicting Semiconductor Behavior and Bandwidths from Crystal Structures and Molecular Orbital Calculations. *J. Am. Chem. Soc.* **2004**, *126*, 15295–15308. [CrossRef]
9. Kunugi, Y.; Takimiya, K.; Toyoshima, Y.; Yamashita, K.; Aso, Y.; Otsubo, T. Vapour deposited films of quinoidal biselenophene and bithiophene derivatives as active layers of n-channel organic field-effect transistors. *J. Mater. Chem.* **2004**, *14*, 1367. [CrossRef]
10. Takahashi, T.; Matsuoka, K.-I.; Takimiya, K.; Otsubo, T.; Aso, Y. Extensive Quinoidal Oligothiophenes with Dicyanomethylene Groups at Terminal Positions as Highly Amphoteric Redox Molecules. *J. Am. Chem. Soc.* **2005**, *127*, 8928–8929. [CrossRef]
11. Handa, S.; Miyazaki, E.; Takimiya, K.; Kunugi, Y. Solution-Processible n-Channel Organic Field-Effect Transistors Based on Dicyanomethylene-Substituted Terthienoquinoid Derivative. *J. Am. Chem. Soc.* **2007**, *129*, 11684–11685. [CrossRef] [PubMed]
12. Ribierre, J.C.; Fujihara, T.; Watanabe, S.; Matsumoto, M.; Muto, T.; Nakao, A.; Aoyama, T. Direct Laser Writing of Complementary Logic Gates and Lateral p-n Diodes in a Solution-Processible Monolithic Organic Semiconductor. *Adv. Mater.* **2010**, *22*, 1722–1726. [CrossRef] [PubMed]
13. Yamamoto, K.; Ie, Y.; Nitani, M.; Tohnai, N.; Kakiuchi, F.; Zhang, K.; Pisula, W.; Asadi, K.; Blom, P.W.M.; Aso, Y. Oligothiophene quinoids containing a benzo[c]thiophene unit for the stabilization of the quinoidal electronic structure. *J. Mater. Chem. C* **2018**, *6*, 7493–7500. [CrossRef]
14. Yamamoto, K.; Kato, S.; Zajaczkowska, H.; Marszalek, T.; Blom, P.W.M.; Ie, Y. Effects of fluorine substitution in quinoidal oligothiophenes for use as organic semiconductors. *J. Mater. Chem. C* **2020**, *8*, 3580–3588. [CrossRef]
15. Moles Quintero, S.; Zafra, J.L.; Yamamoto, K.; Aso, Y.; Ie, Y.; Casado, J. Oligoene and cyanine features of tetracyano quinoidal oligothiophenes. *J. Mater. Chem. C* **2021**, *9*, 10727–10740. [CrossRef]
16. Casado, J.; Miller, L.L.; Mann, K.R.; Pappenfus, T.M.; Higuchi, H.; Ortí, E.; Milián, B.; Pou-Amérigo, R.; Hernández, V.; López Navarrete, J.T. Quinonoid Oligothiophenes as Electron-Donor and Electron-Acceptor Materials. A Spectroelectrochemical and Theoretical Study. *J. Am. Chem. Soc.* **2002**, *124*, 12380–12388. [CrossRef]
17. Ponce Ortiz, R.; Casado, J.; Rodríguez González, S.; Hernández, V.; López Navarrete, J.T.; Viruela, P.M.; Ortí, E.; Takimiya, K.; Otsubo, T. Quinoidal oligothiophenes: Towards biradical ground-state species. *Chem.—A Eur. J.* **2010**, *16*, 470–484. [CrossRef] [PubMed]
18. Casado, J.; Hernández, V.; López Navarrete, J.T. Vibrational Raman Shifts and Aromaticity: The Case of Oligothiophenes. *Chem. Rec.* **2015**, *15*, 1110–1118. [CrossRef]

19. Casado, J. Para-Quinodimethanes: A Unified Review of the Quinoidal-Versus-Aromatic Competition and its Implications. *Top. Curr. Chem.* **2017**, *375*, 73. [CrossRef]
20. Ponce Ortiz, R.; Casado, J.; Hernández, V.; López Navarrete, J.T.; Viruela, P.M.; Ortí, E.; Takimiya, K.; Otsubo, T. On the biradicaloid nature of long quinoidal oligothiophenes: Experimental evidence guided by theoretical studies. *Angew. Chem. Int. Ed.* **2007**, *46*, 9057–9061. [CrossRef]
21. Casado, J.; Ponce Ortiz, R.; López Navarrete, J.T. Quinoidal oligothiophenes: New properties behind an unconventional electronic structure. *Chem. Soc. Rev.* **2012**, *41*, 5672–5686. [CrossRef] [PubMed]
22. Fazzi, D.; Canesi, E.V.; Negri, F.; Bertarelli, C.; Castiglioni, C. Biradicaloid Character of Thiophene-Based Heterophenoquinones: The Role of Electron–Phonon Coupling. *ChemPhysChem* **2010**, *11*, 3685–3695. [CrossRef] [PubMed]
23. Casado, J.; López Navarrete, J.T. The longest quinoidal oligothiophene: A Raman story. *Chem. Rec.* **2011**, *11*, 45–53. [CrossRef] [PubMed]
24. Castiglioni, C.; López Navarrete, J.T.; Zerbi, G.; Gussoni, M. A simple interpretation of the vibrational spectra of undoped, doped and photoexcited polyacetylene: Amplitude mode theory in the GF formalism. *Solid State Commun.* **1988**, *65*, 625–630. [CrossRef]
25. Zerbi, G.; Castiglioni, C.; López Navarrete, J.T.; Bogang, T.; Gussoni, M. A molecular viewpoint of lattice dynamics and spectra of conducting polymers. *Synth. Met.* **1989**, *28*, D359–D368. [CrossRef]
26. Castiglioni, C.; Tommasini, M.; Zerbi, G. Raman spectroscopy of polyconjugated molecules and materials: Confinement effect in one and two dimensions. *Philos. Trans. R. Soc. A Math. Phys. Eng. Sci.* **2004**, *362*, 2425–2459. [CrossRef]
27. Zerbetto, F.; Zgierski, M.Z.; Negri, F.; Orlandi, G. Theoretical study of the force fields of the three lowest singlet electronic states of linear polyenes. *J. Chem. Phys.* **1988**, *89*, 3681–3688. [CrossRef]
28. Negri, F.; Orlandi, G.; Zerbetto, F.; Zgierski, M.Z. Theoretical study of the force field of the lowest singlet electronic states of long polyenes. *J. Chem. Phys.* **1989**, *91*, 6215–6224. [CrossRef]
29. Negri, F.; Zgierski, M.Z. The vibronic structure of the S_0 <-> S_1 and S_0 <-> S_2 transitions in simple oligomers of thiophene. *J. Chem. Phys.* **1994**, *100*, 2571–2587. [CrossRef]
30. Medina Rivero, S.; Canola, S.; Zeng, W.; Ramírez, F.J.; Zafra, J.L.; Wu, J.; Negri, F.; Casado, J. Long rylene nanoribbons express polyacetylene-like signatures at their edges. *Phys. Chem. Chem. Phys.* **2019**, *21*, 7281–7287. [CrossRef]
31. González-Cano, R.C.; Di Motta, S.; Zhu, X.; López Navarrete, J.T.; Tsuji, H.; Nakamura, E.; Negri, F.; Casado, J. Carbon-Bridged Phenylene-Vinylenes: On the Common Diradicaloid Origin of Their Photonic and Chemical Properties. *J. Phys. Chem. C* **2017**, *121*, 23141–23148. [CrossRef]
32. Lahti, P.M.; Ichimura, A.S.; Sanborn, J.A. Methodologies for Computational Studies of Quininoidal Diiminediyls: Biradical vs Dinitrene Behavior. *J. Phys. Chem. A* **2001**, *105*, 251–260. [CrossRef]
33. Albrecht, A.C. On the Theory of Raman Intensities. *J. Chem. Phys.* **1961**, *34*, 1476–1484. [CrossRef]
34. Guthmuller, J. Comparison of simplified sum-over-state expressions to calculate resonance Raman intensities including Franck-Condon and Herzberg-Teller effects. *J. Chem. Phys.* **2016**, *144*, 064106. [CrossRef]
35. Guthmuller, J. The role of Herzberg-Teller effects on the resonance Raman spectrum of trans -porphycene investigated by time dependent density functional theory. *J. Chem. Phys.* **2018**, *148*, 124107. [CrossRef]
36. Michl, J.; Bonačić-Koutecký, V. Biradicals and biradicaloids: A unified view. *Tetrahedron* **1988**, *44*, 7559–7585. [CrossRef]
37. Canola, S.; Casado, J.; Negri, F. The double exciton state of conjugated chromophores with strong diradical character: Insights from TDDFT calculations. *Phys. Chem. Chem. Phys.* **2018**, *20*, 24227–24238. [CrossRef]
38. Canola, S.; Dai, Y.; Negri, F. The Low Lying Double-Exciton State of Conjugated Diradicals: Assessment of TDUDFT and Spin-Flip TDDFT Predictions. *Computation* **2019**, *7*, 68. [CrossRef]
39. Negri, F.; Canola, S.; Dai, Y. Spectroscopy of Open-Shell Singlet Ground-State Diradicaloids: A Computational Perspective. In *Diradicaloids*; Wu, J., Ed.; Jenny Stanford Publishing: New York, NY, USA, 2022; pp. 145–179. ISBN 978-981-4968-08-9.
40. Suzuki, Y.; Miyazaki, E.; Takimiya, K. ((Alkyloxy)carbonyl)cyanomethylene-substituted thienoquinoidal compounds: A New class of soluble n-channel organic semiconductors for air-stable organic field-effect transistors. *J. Am. Chem. Soc.* **2010**, *132*, 10453–10466. [CrossRef]
41. Thorley, K.J.; McCulloch, I. Why are S-F and S-O non-covalent interactions stabilising? *J. Mater. Chem. C* **2018**, *6*, 12413–12421. [CrossRef]
42. Frisch, M.J.; Trucks, G.W.; Schlegel, H.B.; Scuseria, G.E.; Robb, M.A.; Cheeseman, J.R.; Scalmani, G.; Barone, V.; Petersson, G.A.; Nakatsuji, H.; et al. *Gaussian 16*; Gaussian, Inc.: Wallingford, CT, USA, 2016.
43. Marian, C.M.; Heil, A.; Kleinschmidt, M. The DFT/MRCI method. *WIREs Comput. Mol. Sci.* **2019**, *9*, 1–31. [CrossRef]
44. Yamaguchi, K. The electronic structures of biradicals in the unrestricted Hartree-Fock approximation. *Chem. Phys. Lett.* **1975**, *33*, 330–335. [CrossRef]
45. Neese, F.; Wennmohs, F.; Becker, U.; Riplinger, C. The ORCA quantum chemistry program package. *J. Chem. Phys.* **2020**, *152*, 224108. [CrossRef] [PubMed]
46. Malagoli, M.; Coropceanu, V.; Da Silva Filho, D.A.; Brédas, J.L. A multimode analysis of the gas-phase photoelectron spectra in oligoacenes. *J. Chem. Phys.* **2004**, *120*, 7490–7496. [CrossRef]
47. Negri, F.; Zgierski, M.Z. Franck-Condon analysis of the S0→T1 absorption and phosphorescence spectra of biphenyl and bridged derivatives. *J. Chem. Phys.* **1992**, *97*, 7124–7136. [CrossRef]

48. Di Motta, S.; Negri, F.; Fazzi, D.; Castiglioni, C.; Canesi, E.V. Biradicaloid and Polyenic Character of Quinoidal Oligothiophenes Revealed by the Presence of a Low-Lying Double-Exciton State. *J. Phys. Chem. Lett.* **2010**, *1*, 3334–3339. [CrossRef]
49. Di Donato, E.; Vanzo, D.; Semeraro, M.; Credi, A.; Negri, F. Tuning Fluorescence Lifetimes through Changes in Herzberg−Teller Activities: The Case of Triphenylene and Its Hexamethoxy-Substituted Derivative. *J. Phys. Chem. A* **2009**, *113*, 6504–6510. [CrossRef]
50. Guthmuller, J.; Champagne, B. Resonance Raman scattering of rhodamine 6G as calculated by time-dependent density functional theory: Vibronic and solvent effects. *J. Phys. Chem. A* **2008**, *112*, 3215–3223. [CrossRef]